nature neuroscience

One-step optogenetics with multifunctional flexible polymer fibers

Seongjun Park[1,2], Yuanyuan Guo[3–5], Xiaoting Jia[5], Han Kyoung Choe[6], Benjamin Grena[2,3], Jeewoo Kang[7], Jiyeon Park[8], Chi Lu[2,3], Andres Canales[2,3], Ritchie Chen[2,3], Yeong Shin Yim[6], Gloria B Choi[6], Yoel Fink[2,3] & Polina Anikeeva[2,3]

Optogenetic interrogation of neural pathways relies on delivery of light-sensitive opsins into tissue and subsequent optical illumination and electrical recording from the regions of interest. Despite the recent development of multifunctional neural probes, integration of these modalities in a single biocompatible platform remains a challenge. We developed a device composed of an optical waveguide, six electrodes and two microfluidic channels produced via fiber drawing. Our probes facilitated injections of viral vectors carrying opsin genes while providing collocated neural recording and optical stimulation. The miniature (<200 μm) footprint and modest weight (<0.5 g) of these probes allowed for multiple implantations into the mouse brain, which enabled opto-electrophysiological investigation of projections from the basolateral amygdala to the medial prefrontal cortex and ventral hippocampus during behavioral experiments. Fabricated solely from polymers and polymer composites, these flexible probes minimized tissue response to achieve chronic multimodal interrogation of brain circuits with high fidelity.

With its genetic precision and millisecond resolution[1], optogenetics is an indispensable tool in neuroscience for correlating the electrophysiological contributions of specific cell types to observed behaviors[2,3]. As this method depends on the expression of light-sensitive microbial opsins in genetically identifiable neuronal populations[4], viral vectors must be infused directly into neural tissue. Opsins typically exhibit activation spectra in the visible range, where scattering properties of biological matter limit the penetration depth to <1 mm (ref. 5), which necessitates implantation of light sources and additional hardware for electrophysiological readout. Although substantial progress has been made to engineer flexible[6], multifunctional and wireless probes with viral delivery and optical stimulation capabilities[7,8], integration of a recording functionality into these platforms continues to be a technological challenge. The development of such an integrated device is further complicated by the foreign body reaction to implanted probes, which stems from acute[9] and chronic[10] tissue damage that scale with the probe size and stiffness, respectively[11].

We developed miniature and flexible all-polymer integrated probes for behavioral optogenetic studies of neural circuits with reduced mechanical invasiveness. Our probes incorporate recording electrodes, optical waveguides and microfluidic channels, all within the dimensions of silica fibers that are routinely used in optogenetic experiments. To produce these probes, we relied on the thermal drawing process[12,13] that has previously facilitated fabrication of multifunctional devices for neural interfaces[14]. Our probes allowed for one-step surgery, including injection of viral vectors carrying opsin genes into specific locations of the mouse brain, and subsequent recording and optical stimulation of neural activity during free behavior. The small footprint of these devices permitted their implantation into several brain regions, facilitating optical control of behavior and electrophysiological readout of the underlying projection dynamics. With integrated modalities and a miniature footprint, this technology offers a minimally invasive alternative to the multiple-step surgeries that are currently required for optogenetic mapping of brain function.

RESULTS

Design and fabrication of multifunctional fibers with engineered composite electrodes

Conductive polymers and polymer composites offer unmatched tunability in chemical and mechanical properties[15], allowing for precise engineering of materials interfaces with neural tissue to achieve improved long-term recording performance compared with metallic electrodes[16,17]. These materials, however, often exhibit poor conductivity and are incompatible with high-throughput integration techniques[18]. Carbon-loaded polymer composites are characterized by high chemical stability in physiological solutions as well as tunable elastic properties[19,20]. The substantial sheet resistance of commercially

[1]Department of Electrical Engineering and Computer Science, Massachusetts Institute of Technology, Cambridge, Massachusetts, USA. [2]Research Laboratory of Electronics, Massachusetts Institute of Technology, Cambridge, Massachusetts, USA. [3]Department of Materials Science and Engineering, Massachusetts Institute of Technology, Cambridge, Massachusetts, USA. [4]Department of Biomedical Engineering, Tohoku University, Sendai, Miyagi, Japan. [5]Department of Electrical and Computer Engineering, Virginia Polytechnic Institute and State University, Blacksburg, Virginia, USA. [6]McGovern Institute for Brain Research and Department of Brain and Cognitive Sciences, Massachusetts Institute of Technology, Cambridge, Massachusetts, USA. [7]Department of Chemical Engineering, Massachusetts Institute of Technology, Cambridge, Massachusetts, USA. [8]Department of Mechanical Engineering, Massachusetts Institute of Technology, Cambridge, Massachusetts, USA. Correspondence should be addressed to P.A. (anikeeva@mit.edu).

Received 14 June 2016; accepted 23 January 2017; published online 20 February 2017; doi:10.1038/nn.4510

available composites, however, restricts electrode miniaturization as a result of increased impedance, which reduces the ability of these electrodes to detect extracellular potentials.

To substantially improve electrode conductivity, we developed a custom conductive polymer composite comprised of conductive polyethylene (CPE) and 5% graphite (by weight, gCPE; **Fig. 1a**). The sheet resistance of the composite was reduced 4.1-fold when compared with commercially available CPE (0.8 kΩ/□ for gCPE versus 3.3 kΩ/□ for CPE). We hypothesized that the reduced sheet resistance should afford lower electrode dimensions without sacrificing the quality of electrophysiological recordings. Along with a waveguide core (polycarbonate (PC), refractive index n_{PC} = 1.586, glass transition temperature T_g = 150 °C[21]) and cladding (cyclic olefin copolymer (COC), refractive index n_{COC} = 1.53, T_g = 158 °C[22]), we incorporated six gCPE electrodes (melting temperature, T_M~123 °C) into a macroscopic template, a preform, by standard machining to produce a scaled-up version of the desired fiber (**Fig. 1b**). The preform was then heated and stretched into ~100-m-long fiber with preform feature dimensions reduced 50~200-fold (**Fig. 1c–e** and **Supplementary Fig. 1**). By adjusting the drawing parameters, the sizes of electrodes and microfluidic channels were reduced to 20–30 µm, whereas the diameter of the waveguide was tuned between 50–80 µm. The entire integrated structure had a diameter between 180 and 220 µm. (**Fig. 1f**). For our experiments we selected a fiber section with a diameter of 200 µm. In this 10-m-long section the dimensions of the six electrodes were found to be 20.9 ± 1.3 µm, 20.7 ± 0.9 µm, 25.8 ± 1.5 µm, 24.0 ± 1.8 µm, 24.5 ± 1.4 µm and 22.6 ± 2.3 µm; the microfluidic channels had dimensions of 16.4 ± 2.1 µm and 15.3 ± 1.9 µm; and the waveguide diameter measured 68.2 ± 2.9 µm (**Supplementary Fig. 1e**).

Evaluation of mechanical, electrical, optical and microfluidic properties of the fiber

The integrated fiber probes were flexible, with a bending stiffness of 76.1–83.5 N/m in the frequency range of respiration and heartbeat (0.01–10 Hz), which was substantially lower than that of silica optical fibers (93.6–104.8 N/m) of comparable dimensions (**Supplementary Fig. 2a**). As neural interface devices are commonly fixed to the skull, we anticipated that the lower bending stiffness would reduce the repeated tissue damage associated with relative motion of the brain with respect to the skull[23]. The impedance of multifunctional fiber electrodes at 1 kHz was found to be 1.31 ± 0.27 MΩ, and could be further reduced to 0.62 ± 0.23 MΩ by an overnight soak in a phosphate-buffered saline (PBS) solution (**Fig. 1g**,**h**). We observed a similar reduction to 0.67 ± 0.12 MΩ 3 d after implantation into the mouse brain, and the impedance remained consistent over 3 months (0.71 ± 0.13 MΩ; **Supplementary Fig. 2b**). The observed decrease in impedance when compared with commercial CPE electrodes (2.10 ± 0.39 MΩ and 1.83 ± 0.44 MΩ before and after soaking, respectively) could be attributed to the reduced sheet resistance and enhanced porosity of the composite electrodes (**Supplementary Fig. 2c**). Notably, the impedance of the composite gCPE electrodes was dominated by the tip geometry, whereas the impedance of the electrodes produced from commercial CPE was limited by sheet resistance (**Supplementary Fig. 2d**). The impedance of the gCPE electrodes was invariant with respect to 90° bending deformation (**Fig. 1g**), and we observed no current leakage through the polymer cladding (**Supplementary Fig. 2e**,**f**). In addition, cyclic voltammetry curves of the gCPE electrodes exhibited capacitive behavior without any oxidation or reduction peaks in a voltage window exceeding the magnitude of extracellular potentials (**Supplementary Fig. 2g**). The integrated waveguides exhibited relatively flat transmission in the visible spectrum, including the excitation peak of channelrhodopsin 2 (ChR2) at a wavelength, λ, of 473 nm[24] (**Supplementary Fig. 3a**), as well as low transmission loss (<1.5 dB/cm; **Supplementary Fig. 3b**), which was maintained at body temperature (37 °C; **Supplementary Fig. 3c**,**d**), during bending deformation (90–270° angles at radii of curvature 0.5–15 mm) and even following repeated bending cycles (**Supplementary Fig. 3e**,**f**). Transmission loss was also not affected by implantation into the mouse brain for up to 3 months (no longer time points were collected; **Supplementary Fig. 3g**). To confirm the utility of microfluidic channels for delivery of liquids into the brain tissue, we infused a solution of a dye into a brain phantom (0.6% agarose gel; **Fig. 1i**). We observed a return rate of 70–95% of injected fluid at infusion speeds of 1–100 nl/s even during bending deformation (**Fig. 1j**). The maximum amount of fluid contained in a single microfluidic channel of 1-cm-long probe was 7.85 µl (which exceeds the volume of 3 µl that can be safely delivered into a mouse brain[25]); however, an unlimited amount can be delivered by connecting the channels to an external pump via miniature tubing.

Optogenetic interrogation of prefrontal cortex with multifunctional fibers

By integrating recording, optical stimulation and microfluidic capabilities, our probe enabled multiple simultaneous experiments to be conducted following a one-step implantation surgery (**Fig. 2a**). We outfitted thermally drawn multifunctional fibers with ferrules for optical coupling to lasers or light-emitting diodes, pin connectors for electrical readout, and tubing for fluid interfaces, respectively (**Fig. 2b**). The resulting probe weighed 0.3–0.5 g. To evaluate the ability of the fiber probes to mediate opto-electrophysiological interrogation of neural circuits, we implanted these devices into the medial prefrontal cortex (mPFC) of wild-type (WT) mice (**Fig. 2c**). There the integrated microfluidic channels were used to deliver an adeno-associated virus (AAV, serotype 5) carrying the gene for ChR2 fused to the enhanced yellow fluorescent protein (eYFP) under the excitatory neuronal promoter calmodulin kinase II α-subunit (*AAV5-CaMKIIα::ChR2-eYFP*) (**Fig. 2d**). Robust ChR2 expression in the mPFC was observed 2 weeks after the injection, and the extent of expression was proportional to the injection volume (**Fig. 2e** and **Supplementary Fig. 4a**,**b**). By combining the ability to deliver viral vectors through microfluidic channels and to perform neural recording with gCPE electrodes during optical stimulation via integrated PC/COC waveguides, our probes provided an opportunity to investigate the temporal dynamics of the opsin expression in the mouse brain (**Fig. 2f** and **Supplementary Table 1**). To identify the onset of ChR2 expression following the injection of the AAV5 into the mPFC, we recorded electrophysiological signals in the presence of optogenetic stimulation (10 Hz, 8.6 mW/mm^2, 5-ms pulse width). For these stimulation parameters, which are common in optogenetics experiments, we observed optically evoked potentials in the mPFC after 11 ± 2 d (n = 8). As expected, the amplitude of optically evoked signal increased at larger optical powers and longer expression periods (**Supplementary Fig. 4c**).

Qualitatively similar optically evoked responses were found during acute recordings in transgenic Thy1-ChR2-YFP mice during optical stimulation at 10 Hz (**Supplementary Fig. 5a–f**). Stimulation at 100 Hz evoked activity uncorrelated with optical pulses, further confirming the physiological origin of the optically evoked potentials[26] (**Supplementary Fig. 5g–l**). As a third measure ensuring the physiological (rather than optical artifact) nature of our recordings, experiments in WT mice injected with a control virus, *AAV5-CaMKIIα::eYFP*, revealed no neural response to light pulses (**Supplementary Fig. 6**).

To illustrate the utility of the fiber probes for neurobiological experiments, we subjected WT mice implanted with fiber probes

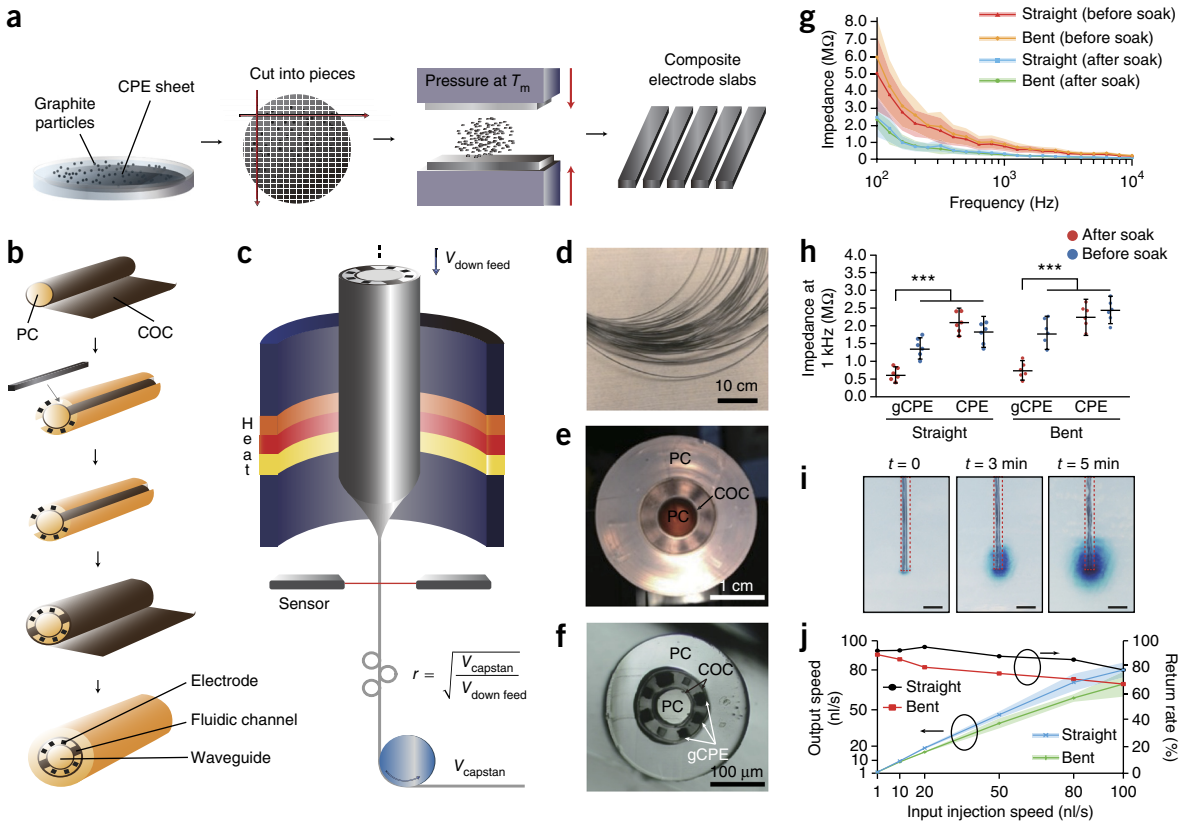

Figure 1 Fabrication and characterization of multifunctional fibers. (**a**) A schematic illustrating fabrication process for gCPE electrodes. (**b**) Fabrication steps involved in assembly of the preform, including a PC waveguide core, COC cladding, gCPE electrodes, hollow channels and protective sacrificial PC cladding. (**c**) An illustration of the fiber drawing process. The diameter of the resulting fiber is determined by the ratio of the capstan and feed speeds and is monitored continuously during the process by a laser sensor. (**d**) Photograph of a bundle of fiber before etching of the sacrificial PC cladding. (**e**) Cross-sectional photograph of the preform before thermal drawing. (**f**) Cross-sectional microscope image of the multimodal fiber produced by thermal drawing of the preform in **e**. (**g**,**h**) Impedance spectra of gCPE electrodes in the multimodal fiber. The impedance was reduced by 24 h soak in PBS. Bending deformation (90°, 2.5 mm radius of curvature) did not appreciably alter impedance spectra ($n = 6$ samples; $^{***}P < 0.001$ determined by one-way ANOVA; flat, $P < 0.0001$, $F_{3,\ 20} = 27.42$; bent, $P < 0.0001$, $F_{3,\ 20} = 21.86$). All error bars and shaded areas in the figure represent s.d. (**i**) Evaluation of microfluidic channels in multimodal fiber via infusion of a dye (BlueJuice) into a phantom brain (0.6% agarose gel). Images are taken at 0, 3 and 5 min after initiation of injection at a speed of 100 nl/min. (**j**) Output speed and return rate measured for microfluidic channel in multifunctional fiber. The microfluidic capability was only slightly reduced during 90° bending deformation ($n = 6$ samples). Shaded areas represent s.d. Scale bars represent 10 cm (**d**), 100 µm (**f**) and 500 µm (**i**).

and transduced with *AAV5-CaMKIIα::ChR2-eYFP* or a control virus *AAV5-CaMKIIα::eYFP* in the mPFC to a standard open field test (OFT, 9-min session, 3-min light OFF/ON/OFF epochs) 6 weeks after surgery. Optical stimulation (5-ms pulse width, 16 mW/mm^2) in mPFC at 20 and 130 Hz resulted in increased velocity ($P < 0.05$) in ChR2-expressing mice as compared with eYFP controls. (**Fig. 2g–j** and **Supplementary Videos 1** and **2**). Consistent with prior experiments[27], there was no change in the time spent in the center of the open field for either group of mice (**Supplementary Fig. 7a**,**b**). In addition to the behavioral manifestation and electrophysiological readout, increased neuronal firing in ChR2-expressing mice was confirmed by the upregulation of an immediate early gene *c-fos* in the mPFC following optical stimulation. No *c-fos* upregulation was observed in control mice (**Supplementary Fig. 7c–e**).

Optical control and electrophysiological readout of projection dynamics with co-implanted fibers

The low footprint of the probes permitted their implantation into multiple brain targets and facilitated opto-electrophysiological projection mapping. In this study, one probe was implanted into the basolateral amygdala (BLA), where it was used for microfluidic delivery of *AAV5-CaMKIIα::ChR2-eYFP* or the control virus (*AAV5-CaMKIIα::eYFP*), and the second identical probe was implanted into either the mPFC[28,29] (**Fig. 3a–d**) or the ventral hippocampus (vHPC)[30] (**Fig. 3e–h**), which are known to receive excitatory projections from the BLA.

Similar to the experiments in the mPFC, we employed the fiber probes to identify the onset of functional ChR2 expression in the BLA and its projection targets (**Supplementary Table 1**). In the BLA, optically evoked (10 Hz, 8.6 mW/mm^2, 5-ms pulse width) neural activity emerged 11 ± 2 d after AAV5 injection ($n = 8$ mice; **Fig. 3i**). In the BLA-to-mPFC projection, optical stimulation evoked a low-latency (5-ms delay with respect to laser pulses) response after 12 ± 1 d ($n = 8$ mice), and an additional response with a longer latency of 32 ms emerged after 15 ± 2 d ($n = 6$ mice; **Fig. 3j** and **Supplementary Fig. 8a**,**b**). The evoked potentials with short latencies are consistent with direct axonal projections from the BLA to mPFC, whereas the long-latency activity may stem from a multi-synaptic network response to optical stimulation in the mPFC[27]. In contrast with stimulation of the BLA inputs in the mPFC, optical excitation in the vHPC evoked only short-latency activity indicative of direct axonal inputs

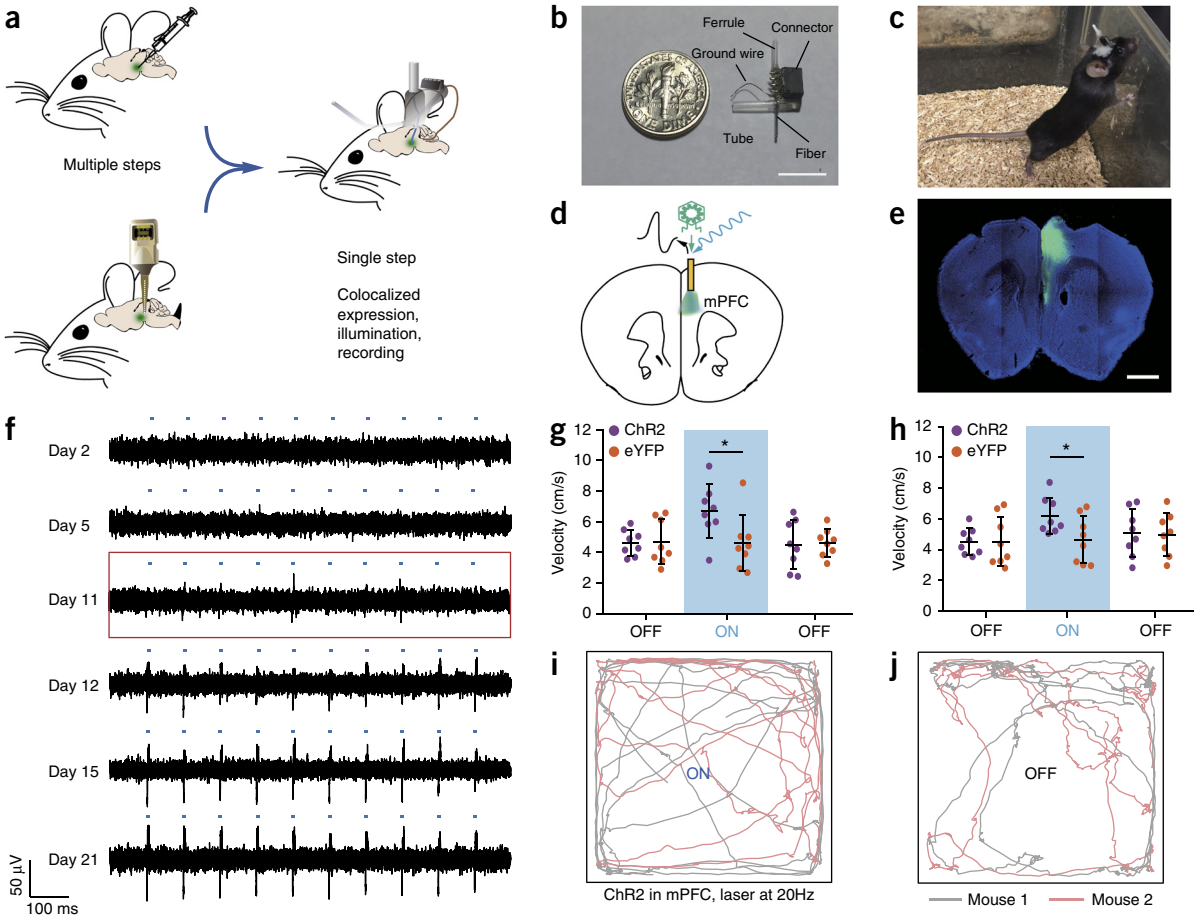

Figure 2 Multifunctional fiber probes enable viral delivery, optical stimulation and recording with a one-step surgery. (**a**) A schematic comparing a traditional two-step surgery for optogenetic experiments and a one-step surgery enabled by a multifunctional fiber probe. (**b**) Picture of a multifunctional fiber probe outfitted with an optical ferrule, electrical connector and an injection tube. The weight of the device varied between 0.3–0.5 g. Scale bar represents 10 mm. (**c**) A WT mouse implanted with a multifunctional probe. (**d**) An illustration of viral delivery (*AAV5-CaMKIIα::ChR2-eYFP*), optical stimulation and electrical recording in mPFC of WT mice with a fiber probe. (**e**) Expression of ChR2-eYFP in the mPFC for a WT mouse 2 weeks after viral transfection. Blue, DAPI; green, eYFP. Scale bar represents 1 mm. (**f**) Electrophysiological recordings during optical stimulation in the mPFC using a fiber probe between 2 and 21 d after transfection with AAV5-CaMKIIα::ChR2-eYFP. (10 Hz, 8.6 mW/mm^2, 5-ms pulse width). Optically evoked potentials were observed 11 ± 2 d following implantation and injection surgery (orange box, $n = 8$ mice). (**g**–**j**) Velocity recorded for WT mice implanted with fiber probes and injected with *AAV5-CaMKIIα::ChR2-eYFP* (or control virus *AAV5-CaMKIIα::eYFP*) in mPFC during OFT. 9-min experiment consisted of 3-min epochs, OFF/ON/OFF optical stimulation: 5-ms pulse width, power density 16 mW/mm^2, and frequency 20 Hz and 130 Hz. (**g**) 20 Hz OFF_pre: $P = 0.9247$, $t = -0.0962$, ON: $P = 0.0352$, $t = 2.3309$, OFF_post: $P = 0.8279$, $t = -0.2215$. (h) 130 Hz OFF_pre: $P = 0.9819$, $t = -0.023$, ON: $P = 0.0417$, $t = 2.2421$, OFF_post: $P = 0.8857$, $t = 0.1464$. d.f. = 14 for all. Error bars represent s.d. (number of animals $n = 8$, $^*P < 0.05$; one-way Student's t test). (**i**,**j**) Representative trajectories for a ChR2 transfected mouse during optical stimulation (5-ms pulse width, 20 Hz) ON (**i**) and OFF (**j**).

from the BLA (**Fig. 3k**). This optically triggered activity could be measured 11 ± 2 d ($n = 8$ mice) after AAV5 injection into the BLA. The faster onset of functional ChR2 expression in the BLA-to-vHPC as compared with BLA-to-mPFC projection could in part be explained by the shorter inter-region distance for the former projection. Similar to the recordings following the direct injection of the AAV5 into the mPFC, the amplitude of the ChR2-mediated signals in the BLA and its projection targets increased with optical power and period of expression (**Supplementary Fig. 8c–e**).

The observed electrophysiological response to optical stimulation of the BLA-to-vHPC projections was further correlated to the behavioral response found in previous studies of this circuit[30]. Specifically, during the OFT (9-min session, 3-min OFF/ON/OFF epochs; **Supplementary Video 3**), mice transfected with ChR2 spent less time in the center of the open field during optical stimulation (20 Hz, 5-ms pulse width) than the control group ($P < 0.05$; **Fig. 3l–n**). The total distance traveled and the average velocity, however, were not modulated by the optical stimulation (**Supplementary Fig. 9a,b**). An increase in *c-fos* expression was observed in the pyramidal layer of vHPC in ChR2-expressing mice, whereas no change was found in the control group (**Supplementary Fig. 9c–h**). Consistent with stimulation of the vHPC, there was no significant change in neuronal *c-fos* levels found in the BLA. To further confirm that the observed behavioral change in response to optical stimulation was a consequence of activation of BLA inputs in the vHPC, we employed fiber probes implanted in the vHPC to deliver an AMPA receptor antagonist, the synaptic blocker 6-cyano-7-nitroquinoxaline-2,3-dione (CNQX). The dose of CNQX was first calibrated by simultaneously performing electrophysiological recording and optical stimulation during the infusion of the drug (**Supplementary Fig. 10**). Following CNQX infusion (0.5 µl, 0.1 mM) into the vHPC, optical stimulation of the BLA terminals did not result in behavioral changes, and ChR2-expressing

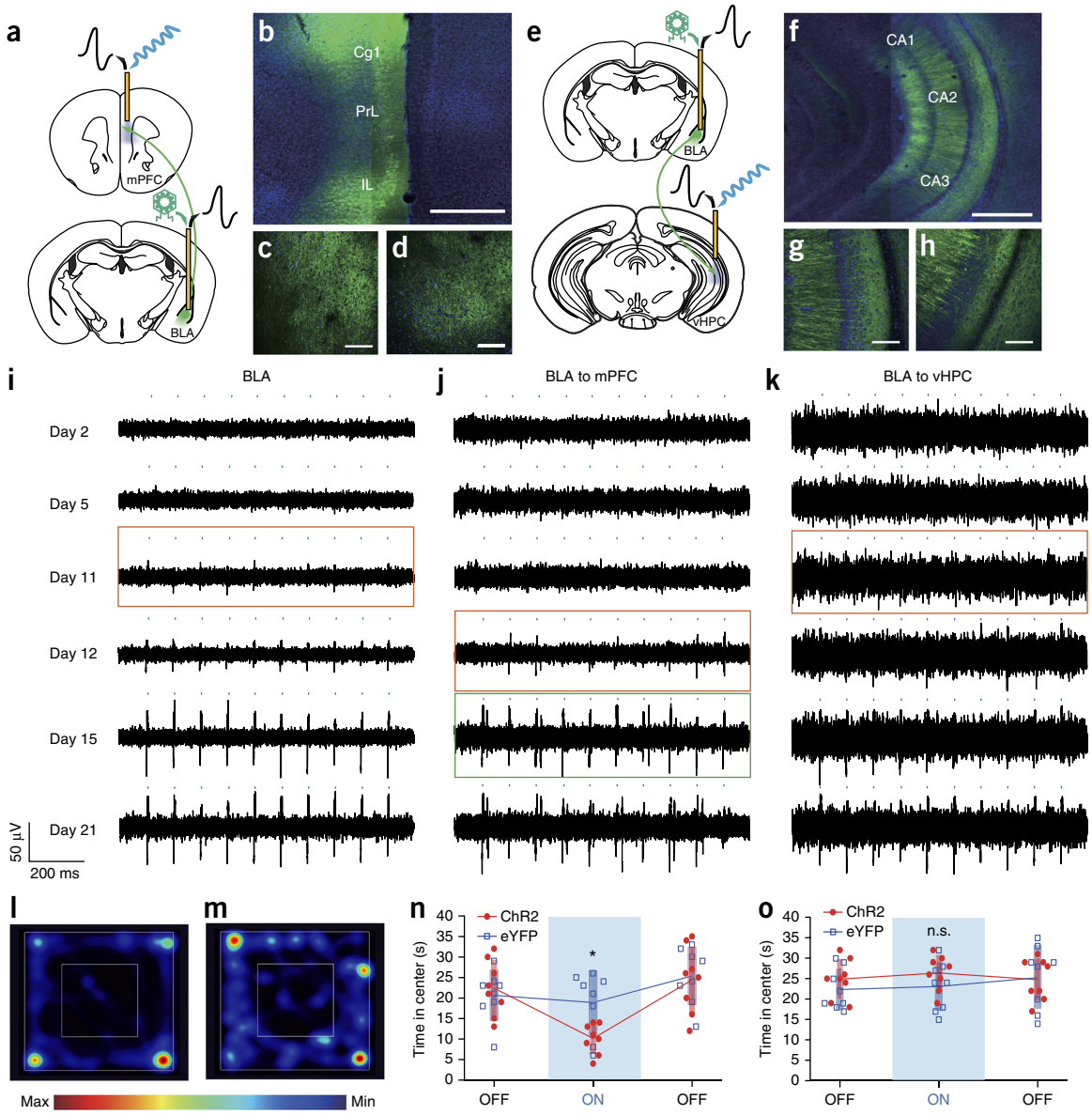

Figure 3 Optogenetic projection mapping using multifunctional fiber probes. (**a**) An illustration of the BLA-to-mPFC projection. *AAV5-CaMKIIα::ChR2-eYFP* was delivered to the BLA, and the optical stimulation and electrical recording were performed in the mPFC. (**b**–**d**) Confocal microscope images of a coronal section containing mPFC 6 weeks after viral transfection in the BLA. (**c**,**d**) Higher magnification images of prelymbic (PrL) and intralymbic (IL) areas of the mPFC. Scale bars are 500 µm (**b**) and 150 µm (**c**,**d**), respectively. (**e**) An illustration of the BLA-to-vHPC projection. Here virus was delivered to BLA and the optical stimulation and electrical recording were performed in the vHPC. (**f**–**h**) Confocal microscope images of a coronal section containing vHPC 6 weeks after viral transfection in the BLA. (**g**,**h**) Higher magnification images of CA2 and CA3 areas of vHPC. Scale bars are 500 µm (**f**) and 150 µm (**g**,**h**), respectively. Blue, DAPI; green, eYFP. (**i**) Electrophysiological recording in the BLA during optical stimulation (10 Hz, 8.6 mW/mm^2, 5-ms pulse width) using a multifunctional fiber performed between 2 and 21 d following transfection with *AAV5-CaMKIIα::ChR2-eYFP*. Optically evoked potentials were observed 11 ± 2 d (orange box, $n = 8$ mice) following surgery. (**j**,**k**) Electrophysiological recordings during optical stimulation using multifunctional fibers implanted in the mPFC (**j**) and vHPC (**k**) between 2 and 21 d after viral transfection using fiber probes implanted in the BLA. Primary low-latency optically evoked potentials were observed following 12 ± 1.4 d (orange box, $n = 8$ mice) for mPFC (**j**) and following 11 ± 2 d (orange box, $n = 8$ mice) for vHPC (**k**). (**j**) For mPFC, secondary long-latency evoked potentials were recorded 15 ± 2 d (green box, $n = 6$ mice) after the surgery. (**l**–**o**) OFT experiments performed in mice implanted with multifunctional fiber probes in vHPC and BLA. 9-min OFT consisted of three 3-min epochs, OFF/ON/OFF optical stimulation (5 ms, 16 mW/mm^2, 20 Hz) in the vHPC. (**l**,**m**) Representative heat map images tracing the position of a mouse transfected with ChR2 during ON (**l**) and OFF (**m**) optical stimulation epochs. (**n**) Time spent in the center of the open field for WT mice transfected in the BLA with *ChR2-eYFP* or *eYFP* alone in the absence or presence of optical stimulation in the vHPC. OFF_pre: $P = 0.5957$, $t = 0.543$, ON: $P = 0.012$, $t = -2.8833$, OFF_post: $P = 0.7947$, $t = -0.2653$. d.f. = 14 for all. (**o**) OFT identical to the one in **l**–**n** performed following delivery of the synaptic blocker CNQX (0.1 mM, 0.5 µl) through a fiber probe implanted in vHPC. OFF_pre: $P = 0.328$, $t = 1.0135$, ON: $P = 0.2319$, $t = 1.2497$, OFF_post: $P = 0.824$, $t = -0.2266$. d.f. = 14 for all. Shaded areas represent s.d. ($n = 8$ mice, $^*P < 0.05$; one way Student's *t* test).

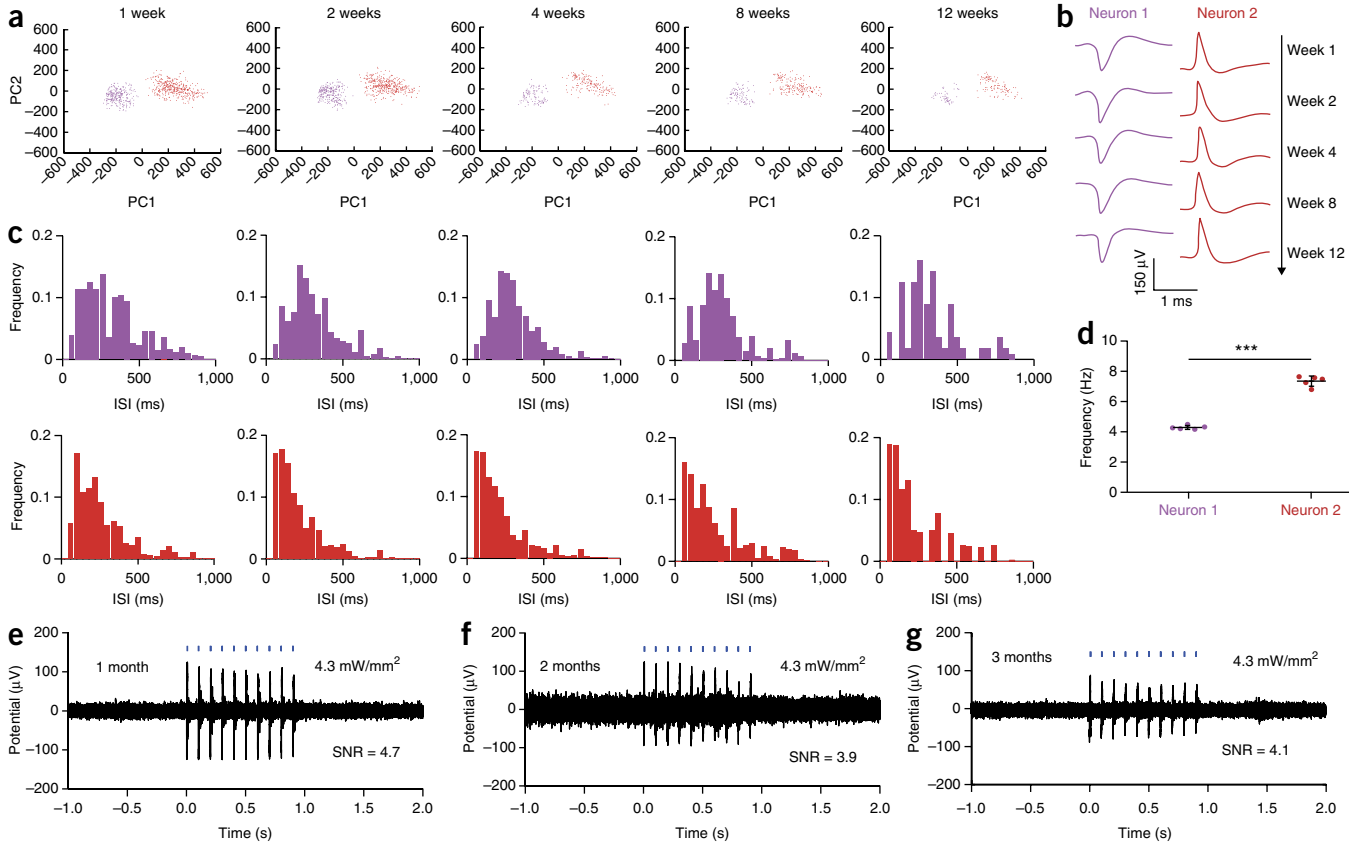

Figure 4 Investigation of single-unit potential with recorded signal from multimodal fiber device. (**a**–**d**) Tracking of isolated single neuron (unit) action potentials (spikes) recorded with a with multifunctional fiber probe in mPFC over a period of 12 weeks following implantation. (**a**) Clusters revealed by PCA of isolated action potentials. (**b**) Average spike waveforms recorded between 1 and 12 weeks corresponding to clusters in **a**. (**c**) ISI histograms for isolated neurons 1 and 2 from **a** and **b**. Maximum histogram interval = 1,000 ms and bin size = 40 ms. (**d**) Average firing frequencies for neurons 1 and 2 obtained from ISI histograms. Significant difference confirmed by one-way Student's *t* test (***$P < 0.001$, $t = 18.7798$, d.f. = 8). Error bars represent s.d. ($n = 5$ samples). (**e**–**g**) Electrophysiological recording of optically evoked potentials in the mPFC of WT mice transfected with *AAV5-CaMKIIα::ChR2-eYFP* performed 1 month (**e**), 2 months (**f**) and 3 months (**g**) after the one-step implantation and transfection surgery. Optical stimulation parameters were fixed at 5-ms pulse width, frequency of 10 Hz and power density 4.3 mW/mm^2.

mice were as likely to spend time in the center of the open field as the control mice during the light stimulation epoch ($P = 0.2319$; **Fig. 3o** and **Supplementary Video 4**).

Assessment of chronic long-term performance and biocompatibility of fiber probes

Given that many neurobiological studies rely on being able to track the activity of identifiable neurons over the course of several weeks, we thought to investigate the ability of fiber probes to record isolated action potentials over a period of 3 months. We found that single neuron (unit) action potentials (spikes) could be isolated from our recordings using principle component analysis (PCA) and that the spike shapes remained stable between 1 and 12 weeks (no longer time points were collected) following fiber probe implantation (**Fig. 4a**,**b**). For the representative units shown in **Figure 4a**,**b**, separation between spike clusters was confirmed by calculating L ratios ($L_{ratio} < 0.01$ for all isolated units; **Supplementary Table 2**). The stability of the clusters was further confirmed by the analysis of the interspike interval (ISI) histograms (maximum interval 1,000 ms, bin size 40 ms; **Fig. 4c**), as well as by calculating the average firing rates. The latter were found to be statistically different for the isolated units ($P < 0.001$; **Fig. 4d**). **Supplementary Figure 11** contains PCA, ISI and firing rate analyses for additional isolated single units recorded from different mice over a period of 12 weeks. In addition to electrophysiological recording, the fiber probes maintained optical stimulation capability for up to 3 months (no longer time points were collected), with no significant decrease in signal to noise ratio (4.7 ± 0.8 for 1 month, 3.9 ± 0.4 for 2 months and 4.1 ± 0.5 for 3 months; **Fig. 4e**–**g**).

We evaluated the biocompatibility of our all-polymer integrated fiber probes by immuno-histochemical quantification of markers characteristic of glial scarring (activated macrophage marker ionized calcium-binding adaptor molecule 1 (Iba1), microglial marker ED1 (staining for macrosialin, CD68), astrocytic marker glial fibrillary acidic protein (GFAP)) and chronic tissue damage associated with the breach of the blood-brain barrier (presence of immunoglobulin G (IgG) in the brain tissue) in coronal brain slices (**Fig. 5** and **Supplementary Fig. 12**)[11,31]. Compared with similarly sized insulated steel microwires (125 µm in diameter), the polymer fibers evoked significantly lower tissue response and blood-brain barrier breach 3 d after implantation ($P < 0.001$ for Iba1 and ED1, $P < 0.01$ for GFAP, and $P < 0.05$ for IgG). The attenuated levels of all markers were found for fiber probes implanted for up to 3 months, whereas significance persisted for the diminished presence of Iba1, GFAP ($P < 0.05$, up to 1 month) and ED1 ($P < 0.05$, up to 2 weeks).

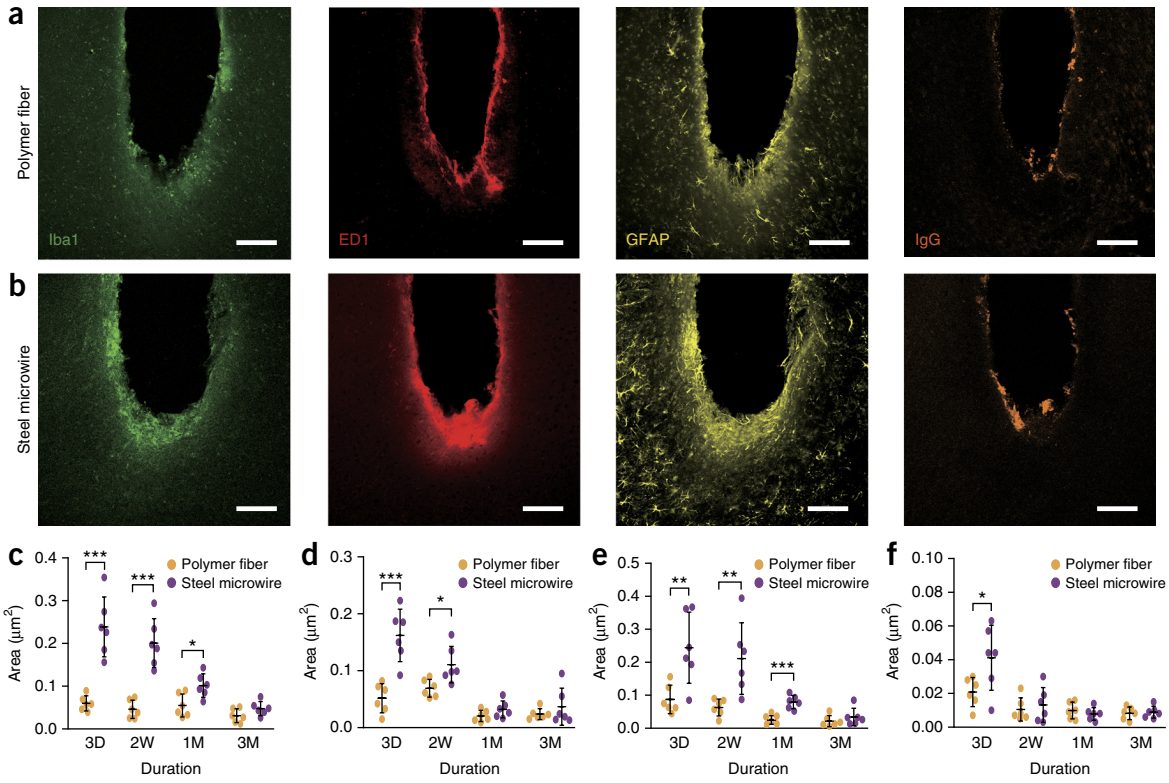

Figure 5 Evaluation of fiber probe and steel microwire biocompatibility using immunohistochemistry in coronal slices. (**a**,**b**) Representative confocal images of glial scarring and blood brain barrier breach surrounding a 200-μm multifunctional fiber probe (**a**) and a 125-μm stainless steel microwire (**b**) 1 month after implantation. Scale bars represent 100 μm. (**c**–**f**) Average fluorescent intensity quantifying the presence of Iba1(**c**), ED1(**d**), GFAP (**e**) and IgG (**f**) for fiber probes and microwires 3 d (3D), 2 weeks (2W), 1 month (1M) and 3 months (3M) after implantation. Iba1, 3 d: $P < 0.001$, $t = -6.0805$; 2 weeks: $P < 0.001$, $t = -6.1953$; 1 month: $P = 0.0144$, $t = -2.9547$; 3 months: $P = 0.1062$, $t = -1.7752$; ED1, 3 d: $P < 0.0001$, $t = -5.1123$; 2 weeks: $P = 0.0174$, $t = -2.8459$; 1 month: $P = 0.1462$, $t = -1.5756$; 3 months: $P = 0.37$, $t = -1.5756$; GFAP, 3 d: $P = 0.0079$, $t = -3.3081$; 2 weeks: $P = 0.0086$, $t = -3.2564$; 1 month: $P < 0.001$, $t = -5.5066$; 3 months: $P = 0.3508$, $t = -0.9787$; IgG, 3 d: $P = 0.0402$, $t = -2.3565$; 2 weeks: $P = -0.6106$, $t = -0.5256$; 1 month: $P = 0.4494$, $t = -0.7872$; 3 months: $P = 0.7569$, $t = -0.3182$. d.f. = 10 for all. Error bars represent s.d. ($n = 6$ samples for each device and time point, $^*P < 0.05$, $^{**}P < 0.01$, $^{***}P < 0.001$; one way Student's t test).

DISCUSSION

Here we combined the fiber drawing process with conductive composite engineering to develop all-polymer miniaturized multifunctional probes for simultaneous optogenetic stimulation, neural recording, and delivery of viral vectors and pharmacological compounds into the mouse brain. Previously, diameters exceeding 400 μm for multifunctional thermally drawn probes were necessitated by comparatively large electrode dimensions designed to compensate for the poor electrical conductivity of commercially available polymer composites. The custom conductive polymer composite (gCPE) that we developed enabled us to reduce electrode dimensions and impedance, allowing for integration of higher density electrophysiology (six electrodes), optical stimulation (a waveguide) and fluid delivery (two channels) in probes with diameters <200 μm, comparable to or smaller than those of silica fibers used for optogenetics. The flexibility and miniature footprint enhanced the biocompatibility of the probes, as indicated by stable long-term recordings of isolated single-neuron action potentials as well as reduced glial response and blood-brain barrier breach 3 months after implantation.

We demonstrated the utility of the miniature and lightweight (<0.5 g) fiber probes by applying them to dynamic opto-electrophysiological study of ChR2 expression in individual brain regions and projection circuits. The latter was enabled by simultaneous implantations of multiple probes. Neural activity correlated with optical stimulation was found 11 d after viral delivery of ChR2 into the mPFC and BLA of WT mice. In mice virally transduced with ChR2 in the BLA, the onset of optically evoked neural activity in the vHPC occurred at 11 d. In the BLA-to-mPFC projection, optical responses were recorded 12 d after viral delivery into the BLA, and additional long-latency responses emerged after 15 d. The observed differences in ChR2 expression in projections could in part be attributed to the proximity of the regions.

Functional expression of ChR2 was further confirmed in behaving mice through observation of increased locomotor activity during optical stimulation in the mPFC of animals virally transduced in this region, as well as through observation of an anxiety phenotype arising during optical stimulation of an established BLA-to-vHPC projection, which could be counteracted by injection of the synaptic blocker CNQX. Although a variety of approaches, such as optogenetics[32,33] and DREADD-facilitated behavioral modulation[34,35] combined with patch-clamp electrophysiology[36,37] in brain slices, are currently employed for functional projection mapping, these techniques do not permit direct correlation of circuit dynamics to observed behavioral outputs. By integrating dense neural recordings with the delivery of transgenes and optical stimuli in a miniature footprint, our device invites multi-site studies of neural projections to probe electrophysiological dynamics underlying a particular neurobiological process or a disease state.

Challenging backend connectorization is a common barrier for widespread neurotechnology adoption in the neuroscience community. Detailed hands-on instructions for connecting our multifunctional fibers to external headstages, light sources and microinjection pumps (**Supplementary Fig. 13**) should allow straightforward assembly of the probes described here without the need for specialized equipment. This should enable a variety of cell-type identification experiments in complex neural circuits[38], where one-step optogenetic capability would ensure one-to-one correspondence of optical and electrophysiological neural interrogation.

METHODS

Methods, including statements of data availability and any associated accession codes and references, are available in the online version of the paper.

Note: Any Supplementary Information and Source Data files are available in the online version of the paper.

ACKNOWLEDGMENTS

The authors are grateful to H. Cho for graphics help during figure preparation. This work was supported in part by the National Institute of Neurological Disorders and Stroke (5R01NS086804, P.A.) National Science Foundation under CAREER award (CBET-1253890, P.A.), Center for Materials Science and Engineering (DMR-1419807, P.A. and Y.F.), Center for Sensorimotor Neural Engineering (EEC-1028725, P.A.) and the McGovern Institute for Brain Research at MIT (P.A. and G.B.C.). S.P. is a recipient of Samsung Scholarship.

AUTHOR CONTRIBUTIONS

S.P., X.J. and P.A. designed the study. B.G. and X.J. designed the conductive polymer composite gCPE. S.P., Y.G. and X.J. fabricated multifunctional fibers. S.P., Y.G., J.P. and J.K. connectorized fibers to optical, electrical and microfluidic interfaces. S.P., Y.G., A.C., C.L. and J.K. characterized the physical properties of fiber probes. S.P. and Y.G. recorded and analyzed the electrophysiological data. G.B.C. facilitated with design and analysis of behavioral experiments. S.P., C.H.K. and Y.S.Y. conducted behavioral tests. S.P. and R.C. performed immunohistochemistry. Y.F. facilitated with fiber design. All of the authors contributed to the writing the manuscript.

COMPETING FINANCIAL INTERESTS

The authors declare no competing financial interests.

1. Boyden, E.S., Zhang, F., Bamberg, E., Nagel, G. & Deisseroth, K. Millisecond-timescale, genetically targeted optical control of neural activity. *Nat. Neurosci.* **8**, 1263–1268 (2005).
2. Tye, K.M. & Deisseroth, K. Optogenetic investigation of neural circuits underlying brain disease in animal models. *Nat. Rev. Neurosci.* **13**, 251–266 (2012).
3. Gradinaru, V., Mogri, M., Thompson, K.R., Henderson, J.M. & Deisseroth, K. Optical deconstruction of parkinsonian neural circuitry. *Science* **324**, 354–359 (2009).
4. Zhang, F., Aravanis, A.M., Adamantidis, A., de Lecea, L. & Deisseroth, K. Circuit-breakers: optical technologies for probing neural signals and systems. *Nat. Rev. Neurosci.* **8**, 577–581 (2007).
5. Aravanis, A.M. *et al.* An optical neural interface: *in vivo* control of rodent motor cortex with integrated fiberoptic and optogenetic technology. *J. Neural Eng.* **4**, S143–S156 (2007).
6. Minev, I.R. *et al.* Biomaterials. Electronic dura mater for long-term multimodal neural interfaces. *Science* **347**, 159–163 (2015).
7. Park, S.I. *et al.* Soft, stretchable, fully implantable miniaturized optoelectronic systems for wireless optogenetics. *Nat. Biotechnol.* **33**, 1280–1286 (2015).
8. Jeong, J.-W. *et al.* Wireless optofluidic systems for programmable *in vivo* pharmacology and optogenetics. *Cell* **162**, 662–674 (2015).
9. Ward, M.P., Rajdev, P., Ellison, C. & Irazoqui, P.P. Toward a comparison of microelectrodes for acute and chronic recordings. *Brain Res.* **1282**, 183–200 (2009).
10. Polikov, V.S., Tresco, P.A. & Reichert, W.M. Response of brain tissue to chronically implanted neural electrodes. *J. Neurosci. Methods* **148**, 1–18 (2005).
11. Lind, G., Linsmeier, C.E. & Schouenborg, J. The density difference between tissue and neural probes is a key factor for glial scarring. *Sci. Rep.* **3**, 2942 (2013).
12. Abouraddy, A.F. *et al.* Towards multimaterial multifunctional fibres that see, hear, sense and communicate. *Nat. Mater.* **6**, 336–347 (2007).
13. Tao, G., Stolyarov, A.M. & Abouraddy, A.F. Multimaterial fibers. *Int. J. Appl. Glass Sci.* **3**, 349–368 (2012).
14. Canales, A. *et al.* Multifunctional fibers for simultaneous optical, electrical and chemical interrogation of neural circuits *in vivo*. *Nat. Biotechnol.* **33**, 277–284 (2015).
15. Guimard, N.K., Gomez, N. & Schmidt, C.E. Conducting polymers in biomedical engineering. *Polym. Biomed. Appl.* **32**, 876–921 (2007).
16. Green, R.A., Lovell, N.H., Wallace, G.G. & Poole-Warren, L.A. Conducting polymers for neural interfaces: challenges in developing an effective long-term implant. *Biomaterials* **29**, 3393–3399 (2008).
17. Kuo, J.T.W. *et al.* Novel flexible Parylene neural probe with 3D sheath structure for enhancing tissue integration. *Lab Chip* **13**, 554–561 (2013).
18. Kim, B.J. *et al.* 3D Parylene sheath neural probe for chronic recordings. *J. Neural Eng.* **10**, 045002 (2013).
19. Huang, J.-C. Carbon black filled conducting polymers and polymer blends. *Adv. Polym. Technol.* **21**, 299–313 (2002).
20. Roy, N., Sengupta, R. & Bhowmick, A.K. Modifications of carbon for polymer composites and nanocomposites. *Prog. Polym. Sci.* **37**, 781–819 (2012).
21. Mark, J.E. *Polymer Data Handbook* (Oxford University Press, 2009).
22. Bäumer, S. *Handbook of Plastic Optics, Second Edition* (Wiley, 2011).
23. Lee, H., Bellamkonda, R.V., Sun, W. & Levenston, M.E. Biomechanical analysis of silicon microelectrode-induced strain in the brain. *J. Neural Eng.* **2**, 81–89 (2005).
24. Nagel, G. *et al.* Channelrhodopsin-2, a directly light-gated cation-selective membrane channel. *Proc. Natl. Acad. Sci. USA* **100**, 13940–13945 (2003).
25. Flecknell, P.A. *Laboratory Animal Anaesthesia* (Elsevier, 2009).
26. Cardin, J.A. *et al.* Targeted optogenetic stimulation and recording of neurons *in vivo* using cell-type-specific expression of Channelrhodopsin-2. *Nat. Protoc.* **5**, 247–254 (2010).
27. Anikeeva, P. *et al.* Optetrode: a multichannel readout for optogenetic control in freely moving mice. *Nat. Neurosci.* **15**, 163–170 (2011).
28. Bacon, S.J., Headlam, A.J.N., Gabbott, P.L.A. & Smith, A.D. Amygdala input to medial prefrontal cortex (mPFC) in the rat: a light and electron microscope study. *Brain Res.* **720**, 211–219 (1996).
29. Lee, B.R. *et al.* Maturation of silent synapses in amygdala-accumbens projection contributes to incubation of cocaine craving. *Nat. Neurosci.* **16**, 1644–1651 (2013).
30. Felix-Ortiz, A.C. *et al.* BLA to vHPC inputs modulate anxiety-related behaviors. *Neuron* **79**, 658–664 (2013).
31. Saxena, T. *et al.* The impact of chronic blood-brain barrier breach on intracortical electrode function. *Biomaterials* **34**, 4703–4713 (2013).
32. Gunaydin, L.A. *et al.* Natural neural projection dynamics underlying social behavior. *Cell* **157**, 1535–1551 (2014).
33. Desai, M. *et al.* Mapping brain networks in awake mice using combined optical neural control and fMRI. *J. Neurophysiol.* **105**, 1393–1405 (2011).
34. Farrell, M.S. *et al.* A Gαs DREADD mouse for selective modulation of cAMP production in striatopallidal neurons. *Neuropsychopharmacology* **38**, 854–862 (2013).
35. Vardy, E. *et al.* A new DREADD facilitates the multiplexed chemogenetic interrogation of behavior. *Neuron* **86**, 936–946 (2015).
36. Nevian, T., Larkum, M.E., Polsky, A. & Schiller, J. Properties of basal dendrites of layer 5 pyramidal neurons: a direct patch-clamp recording study. *Nat. Neurosci.* **10**, 206–214 (2007).
37. Hunt, R.F., Girskis, K.M., Rubenstein, J.L., Alvarez-Buylla, A. & Baraban, S.C. GABA progenitors grafted into the adult epileptic brain control seizures and abnormal behavior. *Nat. Neurosci.* **16**, 692–697 (2013).
38. Kravitz, A.V., Tye, L.D. & Kreitzer, A.C. Distinct roles for direct and indirect pathway striatal neurons in reinforcement. *Nat. Neurosci.* **15**, 816–818 (2012).

ONLINE METHODS

Synthesis of gCPE. CPE (Hillas Packaging) sheets were cut into 9-cm disks. Each disk was weighed and placed into a petri dish. Graphite particles (Sigma) were dissolved in the ethanol (70% by volume), and mixed by a vortex mixer and ultrasonicator. The solution was poured onto CPE sheets (5% graphite by weight relative to CPE), and dried overnight. Following drying disks were weighed again to confirm the graphite content. Several CPE sheets coated with graphite were stacked and consolidated in the hot press at 160 °C forming a 'mille-feuille'-like structure. At high temperature, graphite particles get embedded within the bulk of molten CPE. The first consolidation step creates a heterogeneous CPE composite with non-uniform dispersion of graphite particles. To achieve uniform distribution of graphite within the gCPE composite, the consolidated material was cut into millimeter fragments and subjected to another consolidation step under pressure at 160–180 °C. The latter two steps were repeated 3 times, resulting in a gCPE composite with uniform graphite distribution and sheet resistance significantly lower than that of commercial CPE.

All-polymer multifunctional fiber fabrication. The fibers were produced by thermal drawing from macroscopic templates (preforms). To fabricate a preform, cyclic olefin copolymer (COC; TOPAS) sheets were rolled onto a 16 mm-thick polycarbonate (PC; Ajedium Films) rod, which was followed by several additional PC sheets. Eight rectangular grooves were machined within the outer PC layer, and six of the grooves were filled with gCPE electrodes. Additional COC sheets were wrapped around the structure, followed by several layers of PC that formed a sacrificial cladding that enabled stable processing conditions. The resulting preforms were consolidated under vacuum at 190 °C and then drawn at 240 °C using a custom-built fiber drawing tower as described in prior work[14].

Physical characterization of multifunctional fibers. The bending stiffness of the multifunctional fibers was measured by a dynamic mechanical analyzer (DMA, Q800, TA Instruments) in a single cantilever mode with 50 μm deformation amplitude within the frequency range 0.01–10 Hz. To quantify optical transmission losses, multifunctional fibers were coupled to a diode-pumped solid state (DPSS) laser (Laserglow, 50-mW maximum output, wavelength λ = 473 nm) via ferrules and the light output was measured by photodetector (S121C, 400–1,100 nm, 500 mW, Thorlabs) attached to power meter (PM100D, Thorlabs). Optical transmission was quantified for fiber length between 1–10 cm, bending angles 0°, 90°, 180° and 270°, and radii of curvature 0.5, 1, 2.5, 5, 7.5, 10, 12.5 and 15 mm. Impedance of gCPE electrodes within fiber probes of lengths between 1–10 cm was measured by a LCR meter (HP4284A, Agilent Technologies) using a sinusoidal driving voltage (10 mV, 100 Hz ~10 kHz). Impedance spectra for gCPE electrodes were collected before and after a 24-h soak in PBS. To characterize microfluidic channels, fiber probes were outfitted with external tubing and connected to the standard precision injection apparatus (NanoFil Syringe and UMP-3 Syringe pump, Word Precision Instruments). 10 μl of water was injected with at infusion speeds of 1, 10, 20, 50, 80, and 100 nl/s through the fiber channels, and injection rates were calculated by comparing input and output weight. The injection capability was also confirmed via infusion of the BlueJuice (10×, ThermoFisher Scientific) into 0.6% agarose gel at a speed of 100 nl/min.

Assembly of the multifunctional fiber probes. The sacrificial PC layer was etched by immersion into dichloromethane (Sigma) for 1 min. To establish interfaces with embedded electrodes, the latter were exposed from the cladding manually, and silver paint (SPI Supplies) was used to connect the electrodes to the copper wires. The copper wires were wrapped around the fiber 20 min following the introduction of silver paint to allow for evaporation of the paint thinner. Connections to different electrodes were established at different locations along the fiber probe to avoid cross-talk. The wires were then soldered to the female pin connectors (Digi-Key). An insulated stainless steel ground wire was soldered to one of the pins. Finally, the entire electrode interface region of the fiber probe was coated with 5-min epoxy (Devcon) for mechanical stability and electrical insulation. For microfluidic interfaces, empty channels were exposed manually through the cladding and the entire region was placed within ethylene vinyl acetate tubing (0.5 mm inner diameter, McMaster-Carr) such that the fiber and the tubing were perpendicular to each other, allowing for fluid flow into microfluidic channels through the openings made in the cladding. The tubing was then affixed to the fiber with 5-min epoxy. Optical coupling was established by placing the uppermost part of the fiber into a 6.5-mm-long, 1.25-mm-diameter zirconia ferrule (Thorlabs) and affixing it with optical epoxy (Thorlabs). The ferrule edge was then polished using a Thorlabs fiber polishing kit.

Implantation of fiber probes into mouse brain. All animal procedures were approved by the MIT Committee on Animal Care and carried out in accordance with the National Institutes of Health Guide for the Care and Use of Laboratory Animals. Male C57BL/6 mice aged 6–8 weeks (Jackson Laboratory), and transgenic Thy1-ChR2-YFP mice (donated by G. Feng, Massachusetts Institute of Technology) aged 9–10 weeks were used for the study, and all surgeries were conducted under aseptic conditions. Mice were anaesthetized using via intraperitoneal (IP) injection of ketamine/xylazine mixture in saline (in mg/kg bodyweight: ketamine, 100; xylazine, 10), and then positioned in a stereotactic frame (David Kopf Instruments). A skin incision was made to expose the skull. Lambda and bregma points were used to align the skull with respect to the Mouse Brain Atlas[39]. All implantation and injection coordinates were established according to the brain atlas. The following three types of surgeries were performed: a single injection/implantation in a medial prefrontal cortex (mPFC, coordinates relative to bregma; 1.7 mm anteroposterior (AP); 0.4 mm mediolateral (ML); −1.8 mm dorsoventral (DV)); a viral injection/ implantation of a fiber probe into basolateral amygdala (BLA, −1.6 mm AP; 3.2–3.4 mm ML; −4.9 mm DV) and a concomitant implantation of an identical fiber probe into mPFC (1.7 mm AP; 0.4 mm ML; −1.8 mm DV); a viral injection/ implantation of a fiber probe into BLA and a concomitant implantation of a fiber probe into ventral hippocampus (vHPC, −3.08 mm AP; 3.6–3.7 mm ML; −3.4 mm DV). Adeno-associated viruses serotype 5 (AAV5) carrying *CaMKIIα::hChR2(H134R)-eYFP* and *CaMKIIα::eYFP* plasmids were purchased from University of North Carolina Vector Core at concentrations of 2×10^{12} particles/mL and 3×10^{12} particles/ml respectively. Using a standard microinjection apparatus (NanoFil Syringe and UMP-3 Syringe pump, Word Precision Instruments) 0.5 μl of virus was injected through the microfluidic channels of implanted fiber probes at an infusion rate of 100 nl/min. During injections, the fiber-probes were raised 0.1 mm to accommodate the virus volume. The stainless steel ground wire was soldered to a miniature screw, which was affixed to the skull. Multifunctional probes were fixed to the skull with layer of adhesive (C&B Metabond; Parkell) and dental cement (Jet-Set 4, Lang Dental). Following the surgery and recovery, mice were single housed and were maintained at 22 °C and a 12-h light/dark cycle and provided with food and water *ad libitum*.

***In vivo* electrophysiology.** Multifunctional fiber-probes were attached to PZ2-32 head stage connected to RZ5D electrophysiology system (Tucker Davis Technologies, TDT). For optogenetic stimulation, a DPSS laser (Laserglow Technologies, 50-mW maximum power, wavelength λ = 473 nm) was air-coupled to a silica fiber patchcord, which was then connected to a fiber probe via a ferrule-to-ferrule coupling. For all experiments, pulsed stimulation with 5-ms pulse width was used. Frequencies of 10, 20, 100 and 130 Hz were used. Stimulation was delivered in 1-s stimulation epochs separated by 1-s rest epochs. For the pharmacological experiments, 0.5 μl of CNQX solutions in PBS with concentrations 0.01, 0.05 and 0.1 mM were injected using Nano Fil Syringe and UMP-3 micropump at a speed of 100 nl/min. Following recording, electrophysiological signal was digitized with 50-kHz sampling frequency and filtered in the frequency range 0.3–5 kHz. Spiking activity was detected using commercially available Offline Sorter software (Plexon) with a dead time of 1 ms. Following sorting, spikes were clustered in the first and second principal components (PC1-PC2) plane using k-means clustering, and L ratios for each cluster were calculated using the same software. L ratio < 0.05 is considered characteristic of well-isolated clusteres[40]. ISIs were computed for every neuron, and histograms were plotted by binning the intervals at 40 ms. Firing frequencies were calculated for each neuron by averaging the inverse values of ISIs.

Immunohistochemistry analyses of *c-fos* expression and foreign-body response. For c-fos quantification, mice transfected with *AAV5-CaMKIIα::hChR2(H134R)-eYFP* and *AAV5-CamKIIα::eYFP* were stimulated with 473-nm laser light (16 mW/mm^2, 20 Hz, 5-ms pulse width) for 3 min (1-s ON/OF epochs) and then kept in their home cages for 90 min to allow for c-fos expression. Mice were anesthetized via IP injection of Fatal Plus solution (100 mg/kg in saline), and transcardially perfused with 4% paraformaldehyde (PFA) in PBS.

Brains were extracted and fixed in 4% PFA overnight, and then equilibrated in 30% sucrose in PBS. Samples were randomly allocated within each experimental group. The fixed brains were then sliced into 50 µm coronal sections using a vibrating blade microtome (Leica VT1000S). Sections were then permeabilized and blocked in 0.3% (vol/vol) Triton X-100 and 2.5% (vol/vol) goat serum in PBS for 1 h. This was followed by a 20-h incubation at 4 °C in a solution of primary antibodies (rabbit anti-c-fos[41] 1:500, Calbiochem, PC05) and 2.5% goat serum in PBS. Following incubation, the sections were washed three times for 30 min each with PBS. The slices were then incubated with secondary antibodies (Alexa Fluor 633 goat anti-rabbit 1:500, Life Technologies) for 2 h at 18–25 °C. Following three more washes with PBS, sections were incubated with a nuclear stain DAPI (4′6-diamidino-2-phenylindole) (1:50,000) for 30 min, and washed one more time. PVA-Dabco (Sigma) was used for mounting of slices onto glass microscope slides. A laser scanning confocal microscope (Fluoview FV1000, Olympus) with 4× (air, NA = 0.16), 20× (oil, NA = 0.85) and 60× (oil, NA = 1.42) objectives was used for image acquisition, and overview mosaic images were generated by FV1000 software (Olympus). ImageJ was used to quantify the number of c-fos positive cells in serial z-stack images with a depth of 10 µm. All imaging and analysis was blinded with respect to the experimental conditions. Long-term tissue responses to multimodal fiber probes and similarly sized stainless steel microwires (Good Fellow) were compared at 3 days, 2 weeks, 1 month, and 3 months. Fiber-probes and microwires were implanted to the mPFC region (1.7 AP; ± 0.4 ML; −1.8 DV) of wild type mice (n = 8 per time point, 32 animals, each implanted with 1 fiber probe and 1 microwire). Perfusion, staining and mounting procedures were identical to those described above with the exception of antibodies employed. The primary antibodies were used in the following concentrations: goat anti-GFAP[42] 1:1,000 (Abcam, ab53554); goat anti-Iba1 (ref. 43) 1:500 (Abcam, ab107159); rabbit anti-CD68 (ref. 44) 1:250 (Abcam, ab125212); donkey anti-mouse-IgG conjugated to Alexa Fluor 568 (ref. 45) 1:1,000 (ThermoFisher Scientific, A10037). Secondary antibodies were used in the following concentrations: donkey anti-goat labeled with Alexa Fluor 488 1:1,000 (ThermoFisher Scientific, A11055); or donkey anti-rabbit labeled with Alex Flour 633 1:1,000 (ThermoFisher Scientific, A21070). Confocal images were collected with an oil immersion 20× objective (NA = 0.85). Custom algorithm written in MATLAB (Mathworks) was used to quantify the fluorescence area corresponding to the presence of IgG, GFAP, Iba1, and ED1 (ref. 46). 360 radial lines separated by 1° were distributed from the center of the areas formerly occupied by implants, and the pixel intensity values were found along each line. Two boundary points were determined as 1σ s.d. above average, and total coverage area was calculated within a two-dimensional outline of all end points (720, 2 per line).

Behavioral assays. Behavioral tests were performed by an investigator with knowledge of the identity of the experimental groups versus control groups. For each test, every implanted mouse was randomly allocated to an experimental group before a behavioral experiment. OFTs were conducted with wild type mice receiving optical stimulation coinciding with viral injection in the mPFC (*AAV5-CaMKIIα::hChR2(H134R)-eYFP* or *AAV5-CaMKIIα::eYFP* controls) as well as with wild type mice receiving optical stimulation in the mPFC or in the vHPC with the viruses delivered into the BLA (all implantations and injections are unilateral). For optical stimulation (λ = 473 nm, ~30 mW/mm^2 at the tip of the fiber, 20 Hz, 5-ms pulse width) was delivered through the fiber probes connected via ferrules to silica patch cords coupled to a DPSS laser (Laserglow Technologies). The 50 × 50 cm^2 open field chamber made of white plastic was virtually divided into the center (25 × 25 cm^2) and periphery fields. Mice in their home cages were brought into the room 2 h before starting the experiments. Prior to starting the OFT, mice were placed in the center of the open field for 10 min to recover from handling stress. For *in vivo* pharmacological experiments, 0.5 µl of CNQX solution in PBS (0.1 mM) was injected via a fiber probe implanted in vHPC. OFT sessions consisted of three 3-min epochs (OFF-ON-OFF stimulation, 9 min total), and all trials were recorded by a video camera. All experiments were conducted in the dark, under red light (intensity <10 lx, 650-nm wavelength) to minimize baseline stress associated with background lighting. EthoVision XT (Noldus) software was used for tracking of mouse position, and the location, distance traveled, speed, time spent in each region of the open field were calculated from the tracking data.

Statistical analysis. MATLAB (Mathworks) software was used for assessing the statistical significance of all comparison studies in this work. For fiber characterization experiments, group sizes were determined by power analysis using the *sampsizepwr* function as implemented in the statistical toolbox (α = 0.05, power = 0.9). Power analyses for predetermining sample sizes of immunohistochemistry and behavior test were not performed, instead the group sizes were chosen on the basis of previous research conducted in the same brain region or circuit[27,30]. This was done to enable direct comparison of the observations with the prior work. For all parametric tests, data distribution was assumed to be normal, but this was not formally tested. In the statistical analysis for the characterization of impedance and light transmission, one-way ANOVA followed by Tukey's post-hoc comparison test were conducted with thresholds of $^*P < 0.05$, $^{**}P < 0.01$, $^{***}P < 0.001$. For the comparison between two groups in immunohistochemistry analyses and behavior assays, one-sided Student's t tests were used, and significance threshold was placed at $^*P < 0.05$, $^{**}P < 0.01$. All error bars and shaded areas in the graphs represent s.d.

A **Supplementary Methods Checklist** is available.

Data and code availability. The data supporting the findings of this study are presented within the manuscript and are available from the corresponding author upon request. Samples of multifunctional fibers are available upon request.

39. Paxinos, G. & Franklin, K.B.J. *The Mouse Brain in Stereotaxic Coordinates, 2nd Edition* (Academic Press, 2004).
40. Schmitzer-Torbert, N., Jackson, J., Henze, D., Harris, K. & Redish, A.D. Quantitative measures of cluster quality for use in extracellular recordings. *Neuroscience* **131**, 1–11 (2005).
41. Felix-Ortiz, A.C. & Tye, K.M. Amygdala inputs to the ventral hippocampus bidirectionally modulate social behavior. *J. Neurosci.* **34**, 586–595 (2014).
42. Jukkola, P., Guerrero, T., Gray, V. & Gu, C. Astrocytes differentially respond to inflammatory autoimmune insults and imbalances of neural activity. *Acta Neuropathol. Commun.* **1**, 70 (2013).
43. Shi, P. *et al.* Direct pro-inflammatory effects of prorenin on microglia. *PLoS One* **9**, e92937 (2014).
44. Wes, P.D. *et al.* Tau overexpression impacts a neuroinflammation gene expression network perturbed in Alzheimer's disease. *PLoS One* **9**, e106050 (2014).
45. Siracusa, R. *et al.* The association of palmitoylethanolamide with luteolin decreases neuroinflammation and stimulates autophagy in Parkinson's disease model. *CNS Neurol. Disord. Drug Targets* **14**, 1350–1365 (2015).
46. Park, S. *et al.* Optogenetic control of nerve growth. *Sci. Rep.* **5**, 9669 (2015).

doi:10.1038/nn.4510